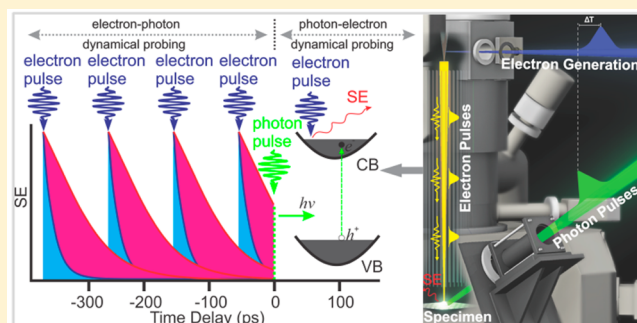


# Real-Space Imaging of Carrier Dynamics of Materials Surfaces by Second-Generation Four-Dimensional Scanning Ultrafast Electron Microscopy

Jingya Sun, Vasily A. Melnikov, Jafar I. Khan, and Omar F. Mohammed\*

Solar and Photovoltaics Engineering Research Center, Division of Physical Sciences and Engineering, King Abdullah University of Science and Technology (KAUST), Thuwal 23955-6900, Kingdom of Saudi Arabia

**ABSTRACT:** In the fields of photocatalysis and photovoltaics, ultrafast dynamical processes, including carrier trapping and recombination on material surfaces, are among the key factors that determine the overall energy conversion efficiency. A precise knowledge of these dynamical events on the nanometer (nm) and femtosecond (fs) scales was not accessible until recently. The only way to access such fundamental processes fully is to map the surface dynamics selectively in real space and time. In this study, we establish a second generation of four-dimensional scanning ultrafast electron microscopy (4D S-UEM) and demonstrate the ability to record time-resolved images (snapshots) of material surfaces with 650 fs and  $\sim 5$  nm temporal and spatial resolutions, respectively. In this method, the surface of a specimen is excited by a clocking optical pulse and imaged using a pulsed primary electron beam as a probe pulse, generating secondary electrons (SEs), which are emitted from the surface of the specimen in a manner that is sensitive to the local electron/hole density. This method provides direct and controllable information regarding surface dynamics. We clearly demonstrate how the surface morphology, grains, defects, and nanostructured features can significantly impact the overall dynamical processes on the surface of photoactive-materials. In addition, the ability to access two regimes of dynamical probing in a single experiment and the energy loss of SEs in semiconductor-nanoscale materials will also be discussed.



Interactions at material surfaces and interfaces have been among the most active areas of research in the past decade.<sup>1–10</sup> This activity can be attributed to the important role that surface reactions play in a wide range of technological applications, including interfacial chemistry, n/p junctions and photovoltaics.<sup>11–15</sup> However, understanding heterogeneous reactions on material surfaces requires both knowledge of the nature of these ultrafast dynamical processes, which can be obtained by femtosecond (fs) laser spectroscopy, and high spatial and temporal control of the material surface after laser-pulse excitation. In the last several decades, time-resolved spectroscopy has often been applied to the study of relaxation pathways, carrier recombination and trapping in condensed matter, at different time scales ranging from fs to microsecond ( $\mu$ s).<sup>16–19</sup> Unfortunately, these techniques are limited by the laser's relatively large penetration depth. As a result, information about the surface dynamics that are critical to the aforementioned applications cannot be accessed, and nanometer (nm)-scale spatial resolution cannot be achieved.

The ability to access carrier dynamics selectively on material surfaces with high spatial and temporal control in a photo-induced reaction is a particularly challenging task that can only be achieved by applying four-dimensional ultrafast electron microscopy (4D UEM) with time-resolved images that have nm and fs spatial and temporal resolutions, respectively. More

specifically, four-dimensional ultrafast transmission electron microscopy<sup>20–31</sup> has been developed as a new method for materials investigations that takes advantage of an unprecedented spatial resolution that cannot be achieved by optical means. Recently, as a new direction in 4D electron microscopy, the first generation of S-UEM with 740 fs and less than 10 nm temporal and spatial resolutions was developed on a scanning electron microscope (SEM) and was reported to be applicable to the visualization of materials dynamics, including surface solvation.<sup>32–34</sup> Although a transmission electron microscope has better spatial resolution, S-UEM has several advantages, including simpler sample preparation, the ability to use a thicker specimen, and considerably better heat dissipation for dynamics studies, which results in a reduction of radiation damage. More importantly, in SEM, a typical detected signal (in a pixel-by-pixel recording) is mainly composed of SEs that are ejected from the material surface. Such a method provides direct access to many fundamental dynamical processes on material surfaces compared to the parallel processing of the image of bulk materials using the primary beam in the transmission mode. It is worth pointing out that spatial and

Received: August 26, 2015

Accepted: September 14, 2015

Published: September 14, 2015

temporal visualization has been extended to ultrafast transient absorption microscopy to image dynamics in nanostructures<sup>35</sup> and long-range carrier transport in semiconductor thin films.<sup>36</sup>

The concept of S-UEM is entirely unique; the spatial resolution is that of a conventional SEM, and the time resolution is determined only by the ultrashort laser pulses involved and electron dispersion (see Figure 1), not by the

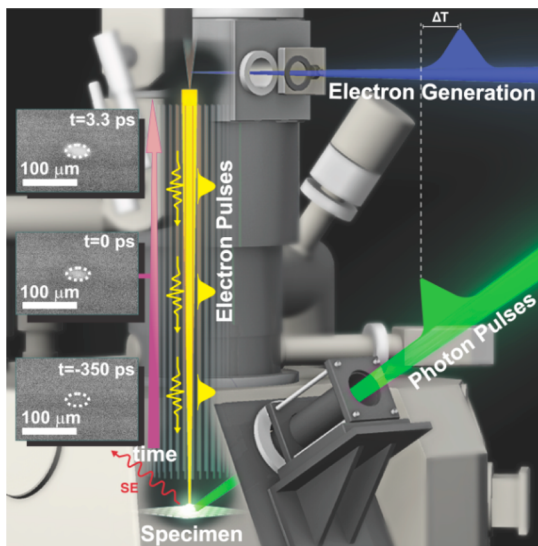


**Figure 1.** Conceptual scheme for scanning ultrafast electron microscopy (S-UEM), showing side-illumination of the field emitter by fs ultraviolet pulses for pulsed electron generation, and the photon pulse for dynamics initiation. A variable optical delay line is used to adjust the arrival time of the pump pulse at the specimen surface, relative to that of the electron probe pulse.

deflection rate<sup>37</sup> or by the streak camera that is commonly used for optical detection.<sup>38</sup> In addition, the SEM can be operated in an environmental mode that allows real-space imaging of the surface stability, including photodegradation and reactivity of photoactive materials under various ambient conditions.

In S-UEM, a laser pulse excites the sample for dynamics initiation, as shown in Figure 1. Subsequently, an electron pulse is generated from the field emission gun by a time-delayed laser pulse and is used as the probe for imaging the carrier density on material surfaces in space and time.

In this contribution, we establish the second generation of S-UEM and provide detailed information regarding pulse characterization, operation modes, laser integration and microscope modification. Due to the absence of a space-charge effect between electrons (results from the low number of electrons/probe pulse), approximately 5 nm and subpicosecond spatiotemporal resolutions are achieved. In one application of this method, we show that carrier trapping and recombination following fs laser excitation can be directly visualized by real-space scanning imaging. We also demonstrate that the morphology, grains, and nanostructure of the material surface can impact the overall relaxation process. Photon-electron dynamical probing (photon pump–electron probe) is a commonly used technique, which we extend by using the electron impact of pulsed primary electrons from an emitter source to examine the dynamics of SE emission from materials surfaces by clocking with timed photon pulses. Such information is entirely new to the UEM methodology and cannot be accessed by any time-resolved techniques or in UEM

that is conducted in transmission mode. Finally, the energy loss of SEs of InGaN nanowires in response to optical excitation is imaged in real space and time.

The primary goal is to conduct pump–probe experiments in electron imaging by converting a continuous electron source into a pulsed emitter and to synchronize the time that the generated pulsed electrons arrive at the sample with the arrival time of a second optical pulse used to initiate dynamics. This provides a new, powerful methodology for imaging dynamical processes in real space and time. The experimental setup can be summarized as follows: the output of a high-powered femtosecond Clark–MXR fiber laser system is integrated with a modified Quanta FEI-650 SEM that is placed on an antivibration module to suppress interference from ambient vibrations. A laser with a 270 fs pulse width delivers IR pulses centered at 1030 nm and can be operated at variable repetition rates ranging from 200 kHz to 25 MHz. The fundamental output was split by 1:1 beam splitter so that it simultaneously pumps two second and third harmonic generators (HG, Clark-MXR) to produce 515 or 343 nm pulses. The output of the first HG (515 or 343 nm) is directed with precision through a pyrometric window and is tightly focused with a 125 mm focal lens onto the cooled Schottky field-emitter tip (zirconium-oxide coated tungsten). This photogenerates electron pulses, which are then accelerated for probing using a 1–30 kV voltage. It is worth mentioning that we refresh the tip every 90 minutes by rising its temperature to ~1800 °C to maintain the high surface quality of the tip. The output of the second HG enters the microscope at a 50° angle relative to the surface normal through a viewport and is focused onto the specimen surface inside the microscope by a 175 mm focal lens for dynamics initiation. A computer-controlled delay line that covers the range of −0.60 to 6.0 ns was used to define the time axis of the time-resolved images recorded. It is worth pointing out that two nanosecond lasers with a delay generator are also integrated into the modified Quanta FEI-650 SEM to extend the dynamical time window to ns and μs time scales when needed. For SEM operation, a working distance of 10 mm from the specimen surface is used throughout the experiment. The pulsed primary electrons from the emitter source will create secondary electrons and backscattered electrons from the surface or the bulk of the specimen as a consequence of the interaction. The SEs are typically generated at a depth of 1 to 5 nm below the sample surface and are subsequently collected by a positively biased Everhart–Thornley detector.<sup>39</sup> The images are obtained either as a single frame with a dwell time of 1 μs at each pixel, or as an integration of 64 frames with a dwell time of 300 ns. This integration suppresses image intensity fluctuations due to the ground and acoustic vibrations. In addition, a contrast-enhanced difference of the SE images from the laser-irradiated and unexcited regions can be extracted by referencing to a negative time frame before the arrival of the excitation pulses (see below). Finally, the time zero between the photon and the electron pulses was first estimated by calculating the travel distance for the two pulses after taking into account the speed difference between the photon and the electron at 30 keV. This is followed by imaging the change in charge distribution of materials surfaces, that is, CdSe or Si single crystals, while scanning the time delay.<sup>34</sup>

The surface phenomenon observed with S-UEM, namely, the formation of bright contrast inside the laser excitation region after optical excitation, can be understood in terms of photon-electron dynamical probing. When the surface of the specimen

(silicon or CdSe single crystals) is excited across the indirect or direct band gap of Si or CdSe single crystals by the 515 nm optical pulse (2.41 eV) used for clocking, an interband carrier transition takes place, and a fraction of the valence-band electrons are promoted to the conduction band. As a result, compared to an unexcited specimen, the promoted electrons have a higher probability of emitting SE above the vacuum level when they are scattered by the energetic primary electron beam. This results in an enhancement (energy gain) of the image contrast (see Figure 2A). Furthermore, the energy gained from the optical excitation may also cause a slight increase in the effective escape depth of the specimen surface and may also enhance SE emission. Interestingly, a dark contrast is observed in the laser-illuminated region when the electron pulse arrives ahead of the optical laser pulse by tens of picoseconds, especially in the case of a CdSe single crystal

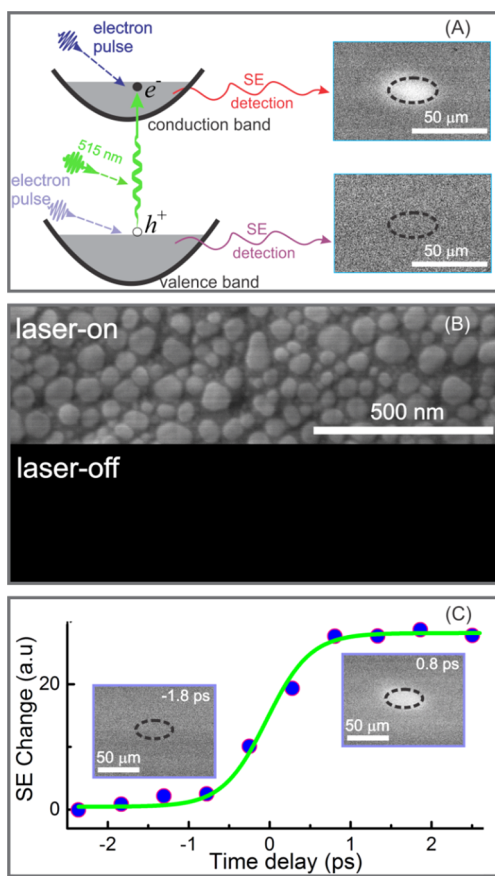


**Figure 2.** (A) Mechanisms for the dynamics observed in S-UEM where the valence band electrons are promoted to the conduction band upon optical excitation and high contrast is recorded due to the energy gain at the center of the excited region. The dashed ellipse indicates the location of the laser on the specimen. (B) S-UEM spatial characteristics (upper) image of gold nanoparticles at 500 nm scale bar from a laser-on scan. From the high resolution image, particles as small as 5 nm diameter could be clearly seen, thus establishing a 5 nm spatial resolution. Finally, a laser-off scan of the same region (lower) shows negligible background intensity, indicating the absence of any contribution from thermal electrons. (C) S-UEM temporal characteristics: Contrast-enhanced difference of the SE images, referenced to a negative time frame directly before and after  $t = 0$ . SE intensity change at the center of the excited region  $s$  as a function of time, obtained using 12 MHz repetition rates. The solid lines are fit to an error function for the dynamics.

( $10\bar{1}0$ ). This new regime of electron–photon dynamical probing will be discussed below.

As stated in the introduction, S-UEM is entirely unique in that it has the spatial resolution of a conventional SEM, and the time resolution is determined only by the duration of the initial photon pump and electron probe pulses. To determine the spatial resolution of our instrument, we imaged Au nanoparticles using three spot-size settings for the SEM and a 2.1 nJ pump pulse energy with a 25 MHz repetition rate to generate pulsed electrons from the emitter tip. As seen in the top panel of Figure 2B, a high quality image with approximately 5 nm spatial resolution can be achieved. It is noteworthy that a laser-off scan of the same image (Figure 2B, lower panel) shows negligible background intensity due to thermal electrons. This indicates that all of the electrons used in taking these images are pulsed. On the other hand, the time resolution of S-UEM does not depend on the response time of the streak camera and the deflection rate that is commonly used for optical detection. Instead, it is determined only by the ultrashort laser pulses involved in time-resolved experiments and is controlled by a optomechanical delay line. As seen in Figure 2C, there is a time-dependent change in a fresh cross section of a CdSe single crystal (0001) in response to optical excitation. This occurs with a rise time of  $650 \pm 100$  fs (obtained from the fit to an error function,  $b + a \text{erf}[(t - t_0)/\tau]$ ), when the pulse energy of the electron-generating pulse was 0.21 nJ before the entrance of the microscope. It should be noted that the temporal resolution of 650 fs is slightly lower than the cross-correlation between the electron probe and the photon pump (~400 fs). This may be originated from the energy spread of pulsed electrons in S-UEM. On the other hand, higher number of photogenerated electrons at the emitter source could cause significant broadening of the temporal profile<sup>40</sup> due to electron–electron repulsion. More specifically, our power dependence experiments performed at a 12 MHz repetition rate indicate that the temporal resolution decreases when the electron density is increased (see Figure 3). The temporal resolution degrades from  $0.65 \pm 0.10$ ,  $0.98 \pm 0.13$ ,  $1.7 \pm 0.20$ , to  $3.2 \pm 0.15$  ps when the number of electrons/pulse (on the specimen) is increased to 5, 10, 20, and 40, which corresponds to pulse energy of 0.21, 0.42, 0.84, and 1.68 nJ, respectively.

Figure 4 shows the dynamical changes in the SE signal for CdSe ( $10\bar{1}0$ ) single crystals (left-panel images) and powder film of the single crystal (right-panel images). It is clear from the figure that there is no change in the difference images that have a large negative time delay (i.e., 350 ps before the arrival of the clocking laser pulse), which is a clear indication that the specimen has relaxed back to its initial state before the next excitation pulse arrives. This shows the reversibility of time-resolved experiments for scanning imaging. On the other hand, immediately after the arrival of the pump pulse, a bright contrast appears within the region of laser irradiation. This increase in the intensity of SE emission results from the promotion of a carrier to the conduction band upon optical excitation. As discussed previously, an interband electronic transition takes place in the photon–electron dynamical probe regime, through the 2.41 eV photoexcitation of an electron across the direct band gap of CdSe (1.73 eV). Higher probability of SE emission is expected for these energetic electrons upon scattering by the pulsed-primary electrons, compared to an unexcited specimen. In addition, due to the energy gain from optical excitation, a slight increase in the effective escape depth is also expected, which causes additional

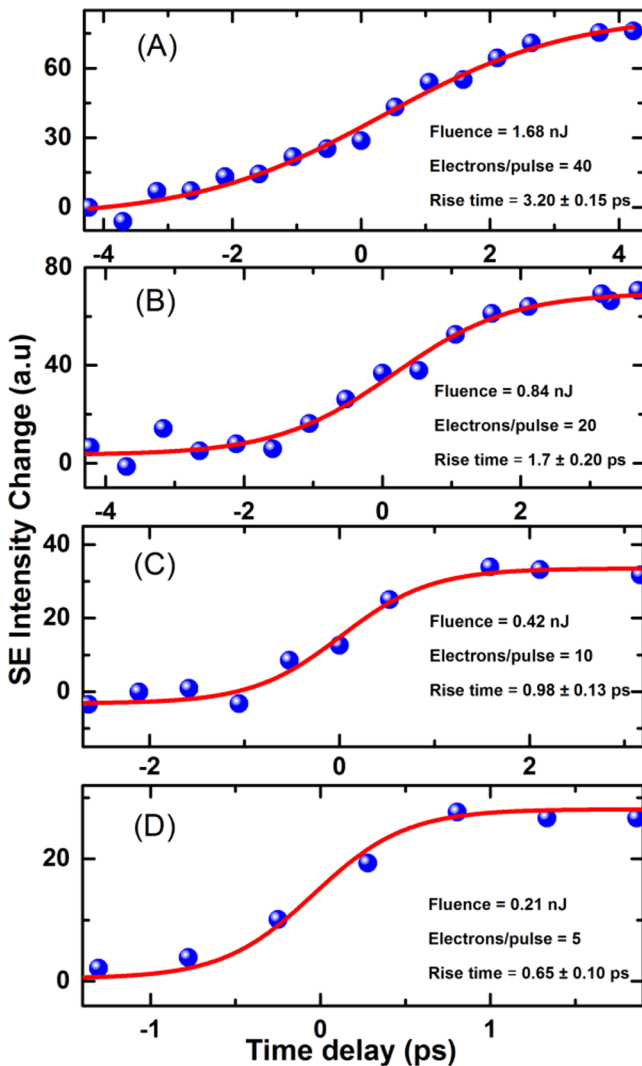


**Figure 3.** SE intensity change at the center of the excited region as a function of the time delay obtained at different fluence values for the electron-generating pulse. Graph shows the sensitivity of the temporal resolution to the number of electrons per pulse. The rise time ranges from 3.2, 1.7, and 0.98 ps to 650 fs, when changing the number of electrons/pulse from 40 (A), 20 (B), and 10 (C) to 5 (D). The solid lines are fit to an error function for the dynamics.

enhancement of the SE emission. Intriguingly, a low contrast is observed in the laser-illuminated region when the electron pulse arrives before the clocking laser pulse at  $-13$  ps time delay (see Figure 4).

This new regime of electron impact is known as electron–photon dynamical probing and is only possible if the later-arriving photons cause a suppression of the SE emission. Because all typical detectors in SEM machines are time-integrating devices,<sup>41</sup> the nature of SE dynamics following the impact of primary electrons has not attracted the attention of the electron microscopy community. In this regime, there are two different mechanisms that may be responsible for the low contrast at negative time delays:

(a) the SE generation delayed in time by backscattered electrons (BSEs) traveling a longer distance from greater bulk depths via inelastic scattering. In this case, when the pump pulse arrives during the dynamical process, it creates additional low-energy electron–hole pairs, and these may act as scattering

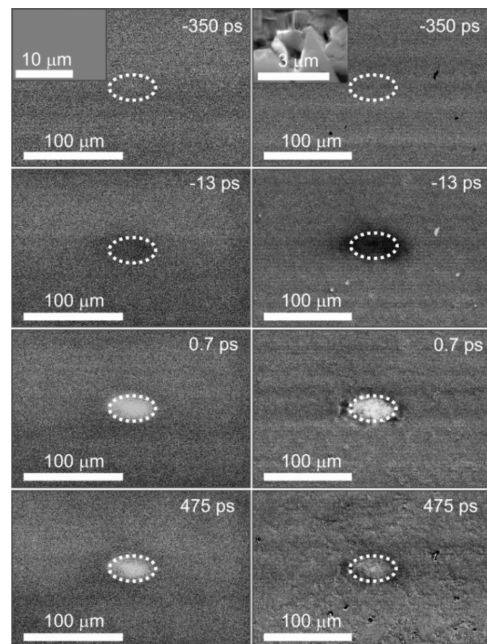


**Figure 4.** Time-resolved difference images of CdSe single crystals at selected time frames, obtained with 30 keV primary electrons (left panel). Time-resolved difference images of the crystalline powder film (made through mechanical grinding of a CdSe single crystal) at selected delay times (right panel). The dashed ellipses indicate the footprint of the clocking optical beam on the specimen. Scanning electron micrographs of the single crystal and the crystalline powder film is shown in the inset, left and right panels, respectively, where more nano- and microstructured features, grains, and defects can be observed on the powder film.

sources that hinder SE generation, causing a dark contrast with a negative time delay of tens of picoseconds. However, we found that the time scale required for BSEs to approach the surface and generate SEs does not support this mechanism. For instance, if we assume that a BSE with an energy of 30 or even 1 keV (with speeds of  $\sim 1 \times 10^8$  and  $1.9 \times 10^7$  m/s, respectively) traveled  $2 \mu\text{m}$ , which is typical depth from which a BSE can be emitted, this implies a decay time of  $\sim 20$  and  $100$  fs, respectively. Based on this information, a decay time of tens of ps cannot be justified or explained by SEs generated by a long-traveling BSE. This indicates that the low contrast observed is due to a slower dynamical process, such as the diffusion process for plasmon-excited carriers (generated by electrons),<sup>42</sup> which can be perturbed by the clocking photon pulse. In this scenario, the typical value for an ambipolar diffusion constant is  $\sim 0.52 \text{ cm}^2/\text{s}$ .<sup>43</sup> If we assume that the 100 or 50 nm ranges constitute the part of the distribution that could eventually contribute to the SE signal, we obtained (using  $L^2/D$ ) a time constant of 192 and 48 ps, respectively. This seems to be a more reasonable explanation for the dark contrast, observed at tens of picoseconds.

(b) If SEs can undergo several scattering processes (i.e., scattering with photoinduced electron/hole) and therefore lose energy while they are migrating toward the specimen surface, a decrease in SE emission is expected and would lead to low contrast. The energy loss for SE is caused mainly by inelastic electron–electron, electron–phonon, and electron–impurity scattering. These three dynamical processes can be distinguished based on their time scales. For instance, electron–electron scattering takes tens of femtoseconds, and electron–

phonon scattering takes a few picoseconds. On the other hand, electron–dopant/impurity scattering is much slower because it may involve carrier trapping and recombination.<sup>32</sup> In this particular case, the corresponding time constant is  $26 \pm 4$  ps and  $50 \pm 10$  ps (see Figure 5, top panel) for single crystal and

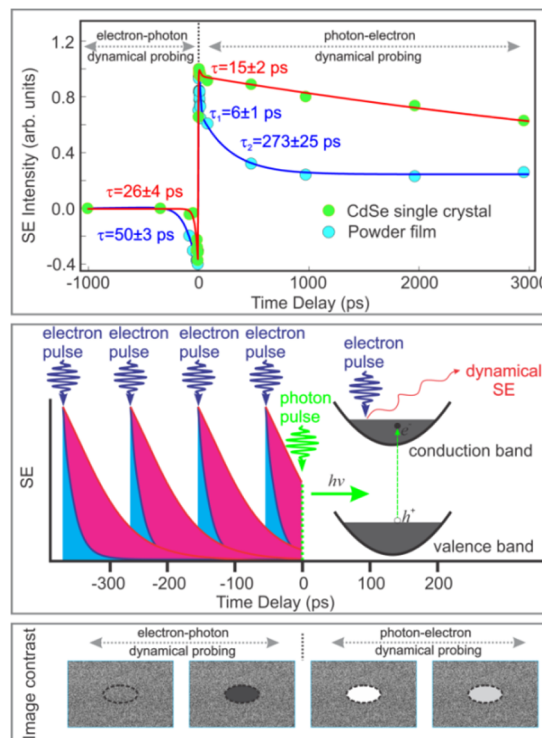


**Figure 5.** (Top panel) dynamics of SE intensities obtained from the center of the excited region for CdSe single crystal (green dots) and the crystalline powder film (blue dots). The solid lines are the results of multiexponential fits. It should be noted that the recovery of the bright contrast to the initial state (signal fades away) is due to the carrier recombination. (Middle panel) Schematic for the information on dynamics obtained in the CdSe single crystals and powder films, in the regimes of electron–photon and photon–electron dynamical probing (see text). Shown in the lower panel are contrast change in the images of the CdSe single crystal and its powder film in the two regimes of probing.

the powder film, respectively, indicating that electron–dopant/impurity scatterings are dominant in the dark contrast images. This change in the SE dynamics can be understood by considering the impurity and dopant atoms and their role as scattering centers that delay SE emission. It should be noted that the impurity, morphological steps, and surface defects can act as additional sources of SE delay in the powder film and may be more important than SE emission compared to the dynamics in the single crystal. This observation provides the direct observation of ultrafast electron-impact dynamics in real space and time.

To confirm that the morphology, grains, and surface defects are key components for controlling the carrier dynamics on materials surfaces, we conducted time-resolved imaging on a crystalline powder film made by mechanical grinding of a CdSe single crystal (see Figure 4, right panel). A fast recovery of the bright contrast is observed due to carrier recombination, with characteristic time constants of 6 and 273 ps. The two time constants can be attributed to different scattering sources, that are, grains, structured features and defects (inset of Figure 4,

right), and thus serve as surface trapping centers to remove a substantial portion of the excited carriers that create high contrast. This surface information cannot be selectively obtained by time-resolved laser spectroscopic techniques because they are limited by the laser's relatively large penetration depth, and therefore, these techniques record mainly bulk information. To conclude this section, two regimes of dynamical probing have been conducted and explained in details for the first time in a single time-resolved experiment, as described in Figure 5, middle and lower panels.

Understanding energy loss mechanisms is crucial for basic understanding and development of semiconductor microelectronic and optoelectronic devices, such as light emitting diodes and laser diodes. In this regime, carrier–carrier scattering and carrier-longitudinal optical (LO) phonon scatterings (electron–phonon, hole–phonon) are the dominant energy loss mechanisms in semiconductors.<sup>44</sup> Typical time scales for these processes range from fs to ps.<sup>45</sup>

These scattering processes lead to spectral broadening and limit the mobility of charge carriers, as well as the speed and efficiency of semiconductor devices.<sup>44,45</sup> Figure 6 shows the

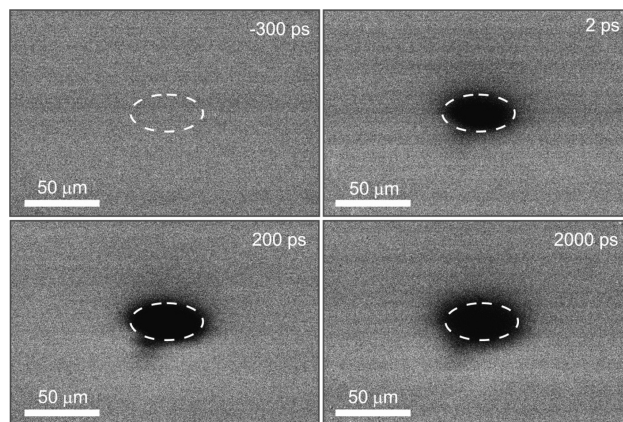


**Figure 6.** Time-resolved difference images for InGaN nanowires at selected time frames upon optical excitation at 515 nm and obtained with 30 keV pulsed primary electrons.

difference SE images for InGaN nanowires after optical excitation at 515 nm. Unlike the case of CdSe and Si, where bright contrast is observed at positive time delays, the measured contrast is dark in this instance. In this case, at positive times, the InGaN nanowire is excited across the band gap (1.62 eV) by the optical pulse and an increase in the electron population of the conduction band will be achieved. However, the promoted electrons are still subject to the scattering processes in the conduction band. Because the effective cross section for the scattering of SEs with conduction electrons is expected to be much higher than that with valence electrons,<sup>32</sup> a decrease in SE emission will give rise to a low contrast. More details, including the mechanism, insights into the carrier–diffusion dynamics, and complementary fs transient absorption spectroscopic data, will be provided in our full account of this work.

In summary, two regimes of dynamical probing can now be differentiated in a single experiment using second generation four-dimensional scanning electron microscopy (S-UEM) developed recently at KAUST. One regime occurs at negative and the other at positive time delays. These are referred to as electron-impact dynamics clocked by photons and photon-electron dynamical probing, respectively. We tested the

capabilities and potential applications of S-UEM in exploring carrier trapping, recombination and SE energy loss on the surface of semiconductor materials. Our time-resolved SE images show how morphological steps, grains, nanostructured features, and defects on material surfaces can control the overall carrier relaxation processes. In addition, an experimental method that uses electrons to initiate dynamics and clocking by photons provides a means of studying the dynamical behavior of secondary electron emission in real time. The methodology and results of the proposed research will have a significant impact on the surface chemistry, photocatalysis, and photovoltaics research communities by providing a method of measuring ultrafast surface dynamics and charge transfer at interfaces in real space and time.

## AUTHOR INFORMATION

### Corresponding Author

\*E-mail: [omar.abdelsaboor@kaust.edu.sa](mailto:omar.abdelsaboor@kaust.edu.sa).

### Notes

The authors declare no competing financial interest.

## ACKNOWLEDGMENTS

The work reported here was supported by King Abdullah University of Science and Technology (KAUST). The authors gratefully acknowledge Dr. R. Bose, Mrs. B. S. Shaheen, and Dr. A. Adhikari for their assistance with the estimation of the temporal resolution of S-UEM. The authors also acknowledge Dr. S.T. Park for reading of the manuscript. O.F.M acknowledges Professor B. S. Ooi for providing InGaN NWs to test with S-UEM.

## REFERENCES

- (1) Suich, D. E.; Caplins, B. W.; Shearer, A. J.; Harris, C. B. Femtosecond Trapping of Free Electrons in Ultrathin Films of NaCl on Ag(100). *J. Phys. Chem. Lett.* **2014**, *5*, 3073–3077.
- (2) Becker, M. A.; Radich, J. G.; Bunker, B. A.; Kamat, P. V. How Does a SILAR CdSe Film Grow? Tuning the Deposition Steps to Suppress Interfacial Charge Recombination in Solar Cells. *J. Phys. Chem. Lett.* **2014**, *5*, 1575–1582.
- (3) Kamat, P. V. Boosting the Efficiency of Quantum Dot Sensitized Solar Cells through Modulation of Interfacial Charge Transfer. *Acc. Chem. Res.* **2012**, *45*, 1906–1915.
- (4) El-Ballouli, A. O.; Alarousu, E.; Bernardi, M.; Aly, S. M.; Lagrow, A. P.; Bakr, O. M.; Mohammed, O. F. Quantum Confinement-Tunable Ultrafast Charge Transfer at the PbS Quantum Dot and Phenyl-C61-butrylic Acid Methyl Ester Interface. *J. Am. Chem. Soc.* **2014**, *136*, 6952–6959.
- (5) Fajardo, A. M.; Lewis, N. S. Rate Constants for Charge Transfer Across Semiconductor-Liquid Interfaces. *Science* **1996**, *274*, 969–972.
- (6) Jung, T. A.; Schlittler, R. R.; Gimzewski, J. K. Conformational Identification of Individual Adsorbed Molecules with the STM. *Nature* **1997**, *386*, 696–698.
- (7) Yang, D.-S.; Mohammed, O. F.; Zewail, A. H. Environmental Scanning Ultrafast Electron Microscopy: Structural Dynamics of Solvation at Interfaces. *Angew. Chem., Int. Ed.* **2013**, *52*, 2897–2901.
- (8) Ayzner, A. L.; Nordlund, D.; Kim, D.-H.; Bao, Z.; Toney, M. F. Ultrafast Electron Transfer at Organic Semiconductor Interfaces: Importance of Molecular Orientation. *J. Phys. Chem. Lett.* **2015**, *6*, 6–12.
- (9) Aly, S. M.; Parida, E. M.; Mohammed, O. F. Ultrafast Electron Injection at the Cationic Porphyrin- Graphene Interface Assisted by Molecular Flattening. *Chem. Commun.* **2014**, *50*, 10452–10455.
- (10) Kraack, J. P.; Lotti, D.; Hamm, P. Ultrafast, Multidimensional Attenuated Total Reflectance Spectroscopy of Adsorbates at Metal Surfaces. *J. Phys. Chem. Lett.* **2014**, *5*, 2325–2329.
- (11) Kiefer, L. M.; King, J. T.; Kubarych, K. J. Dynamics of Rhodium Photocatalysts Revealed through Ultrafast Multidimensional Spectroscopy. *Acc. Chem. Res.* **2015**, *48*, 1123–1130.
- (12) Najafi, E.; Scarborough, T. D.; Tang, J.; Zewail, A. H. Four-Dimensional Imaging of Carrier Interface Dynamics in p-n Junctions. *Science* **2015**, *347*, 164–167.
- (13) Christians, J. A.; Leighton, D. T., Jr.; Kamat, P. V. Rate Limiting Interfacial Hole Transfer in Sb<sub>2</sub>S<sub>3</sub> Solid-State Solar Cells. *Energy Environ. Sci.* **2014**, *7*, 1148–1158.
- (14) Christians, J. A.; Kamat, P. V. Trap and Transfer. Two-Step Hole Injection Across the Sb<sub>2</sub>S<sub>3</sub>/CuSCN Interface in Solid-State Solar Cells. *ACS Nano* **2013**, *7*, 7967–7974.
- (15) O'Donnell, R. M.; Ardo, S.; Meyer, G. J. Charge-Screening Kinetics at Sensitized TiO<sub>2</sub> Interfaces. *J. Phys. Chem. Lett.* **2013**, *4*, 2817–2821.
- (16) Pendlebury, S. R.; Wang, X.; Le Formal, F.; Cornuz, M.; Kafizas, A.; Tilley, S. D.; Graetzel, M.; Durrant, J. R. Ultrafast Charge Carrier Recombination and Trapping in Hematite Photoanodes under Applied Bias. *J. Am. Chem. Soc.* **2014**, *136*, 9854–9857.
- (17) Singh, R. B.; Matsuzaki, H.; Suzuki, Y.; Seki, K.; Minegishi, T.; Hisatomi, T.; Domen, K.; Furube, A. Trapped State Sensitive Kinetics in LaTiO<sub>2</sub>N Solid Photocatalyst with and without Cocatalyst Loading. *J. Am. Chem. Soc.* **2014**, *136*, 17324–17331.
- (18) Wang, L.; McCleese, C.; Kovalsky, A.; Zhao, Y.; Burda, C. Femtosecond Time-Resolved Transient Absorption Spectroscopy of CH<sub>3</sub>NH<sub>3</sub>PbI<sub>3</sub> Perovskite Films: Evidence for Passivation Effect of PbI<sub>2</sub>. *J. Am. Chem. Soc.* **2014**, *136*, 12205–12208.
- (19) Wu, K.; Zhu, H.; Liu, Z.; Rodriguez-Cordoba, W.; Lian, T. Ultrafast Charge Separation and Long-Lived Charge Separated State in Photocatalytic CdS-Pt Nanorod Heterostructures. *J. Am. Chem. Soc.* **2012**, *134*, 10337–10340.
- (20) Barwick, B.; Park, H. S.; Kwon, O.-H.; Baskin, J. S.; Zewail, A. H. 4D Imaging of Transient Structures and Morphologies in Ultrafast Electron Microscopy. *Science* **2008**, *322*, 1227–1231.
- (21) Kwon, O.-H.; Zewail, A. H. 4D Electron Tomography. *Science* **2010**, *328*, 1668–1673.
- (22) Yurtsever, A.; Zewail, A. H. 4D Nanoscale Diffraction Observed by Convergent-Beam Ultrafast Electron Microscopy. *Science* **2009**, *326*, 708–712.
- (23) Flannigan, D. J.; Zewail, A. H. 4D Electron Microscopy: Principles and Applications. *Acc. Chem. Res.* **2012**, *45*, 1828–1839.
- (24) Kwon, O.-H.; Park, H. S.; Baskin, J. S.; Zewail, A. H. Nonchaotic Nonlinear Motion Visualized in Complex Nanostructures by Stereographic 4D Electron Microscopy. *Nano Lett.* **2010**, *10*, 3190–3198.
- (25) Kwon, O.-H.; Ortalan, V.; Zewail, A. H. Macromolecular Structural Dynamics Visualized by Pulsed Dose Control in 4D Electron Microscopy. *Proc. Natl. Acad. Sci. U. S. A.* **2011**, *108*, 6026–6031.
- (26) Ortalan, V.; Zewail, A. H. 4D Scanning Transmission Ultrafast Electron Microscopy: Single-Particle Imaging and Spectroscopy. *J. Am. Chem. Soc.* **2011**, *133*, 10732–10735.
- (27) Park, S. T.; Flannigan, D. J.; Zewail, A. H. Irreversible Chemical Reactions Visualized in Space and Time with 4D Electron Microscopy. *J. Am. Chem. Soc.* **2011**, *133*, 1730–1733.
- (28) Park, S. T.; Flannigan, D. J.; Zewail, A. H. 4D Electron Microscopy Visualization of Anisotropic Atomic Motions in Carbon Nanotubes. *J. Am. Chem. Soc.* **2012**, *134*, 9146–9149.
- (29) Park, S. T.; Yurtsever, A.; Baskin, J. S.; Zewail, A. H. Graphene-Layered Steps and their Fields Visualized by 4D Electron Microscopy. *Proc. Natl. Acad. Sci. U. S. A.* **2013**, *110*, 9277–9282.
- (30) Yurtsever, A.; Baskin, J. S.; Zewail, A. H. Entangled Nanoparticles: Discovery by Visualization in 4D Electron Microscopy. *Nano Lett.* **2012**, *12*, 5027–5032.
- (31) Plemmons, D. A.; Suri, P. K.; Flannigan, D. J. Probing Structural and Electronic Dynamics with Ultrafast Electron Microscopy. *Chem. Mater.* **2015**, *27*, 3178–3192.

- (32) Cho, J.; Hwang, T. Y.; Zewail, A. H. Visualization of Carrier Dynamics in p(n)-Type GaAs by Scanning Ultrafast Electron Microscopy. *Proc. Natl. Acad. Sci. U. S. A.* **2014**, *111*, 2094–2099.
- (33) Yang, D.-S.; Mohammed, O. F.; Zewail, A. H. Environmental Scanning Ultrafast Electron Microscopy: Structural Dynamics of Solvation at Interfaces. *Angew. Chem., Int. Ed.* **2013**, *52*, 2897–2901.
- (34) Mohammed, O. F.; Yang, D.-S.; Pal, S. K.; Zewail, A. H. 4D Scanning Ultrafast Electron Microscopy: Visualization of Materials Surface Dynamics. *J. Am. Chem. Soc.* **2011**, *133*, 7708–7711.
- (35) Lo, S. S.; Shi, H. Y.; Huang, L.; Hartland, G. V. Imaging the Extent of Plasmon Excitation in Au Nanowires using Pump-Probe Microscopy. *Opt. Lett.* **2013**, *38*, 1265–1267.
- (36) Guo, Z.; Manser, J. S.; Wan, Y.; Kamat, P. V.; Huang, L. Spatial and Temporal Imaging of Long-Range Charge Transport in Perovskite Thin Films by Ultrafast Microscopy. *Nat. Commun.* **2015**, *6*, 7471.
- (37) Macdonal, N. C.; Robinson, G. Y.; White, R. M. Time-Rsolved Scanning Electron Microscopy and its Application to Bulk-Effect Oscillators. *J. Appl. Phys.* **1969**, *40*, 4516–4528.
- (38) Merano, M.; Sonderegger, S.; Crottini, A.; Collin, S.; Renucci, P.; Pelucchi, E.; Malko, A.; Baier, M. H.; Kapon, E.; Deveaud, B.; et al. Probing Carrier Dynamics in Nanostructures by Picosecond Cathodoluminescence. *Nature* **2005**, *438*, 479–482.
- (39) Yang, D.-S.; Mohammed, O. F.; Zewail, A. H. Scanning Ultrafast Electron Microscopy. *Proc. Natl. Acad. Sci. U. S. A.* **2010**, *107*, 14993–14998.
- (40) Gahlmann, A.; Park, S. T.; Zewail, A. H. Ultrashort Electron Pulses for Diffraction, Crystallography and Microscopy: Theoretical and Experimental Resolutions. *Phys. Chem. Chem. Phys.* **2008**, *10*, 2894–2909.
- (41) Goldstein, J. I.; Newbury, D. E.; Joy, D. C.; Lyman, C. E.; Echlin, P.; Lifshin, E.; Sawyer, L.; Michael, J. R. *Scanning Electron Microscopy and X-ray Microanalysis*, 3rd ed.; Springer: New York, 2003.
- (42) Reimer, L.: *Scanning Electron Microscopy: Physics of Image Formation and Microanalysis*, 2nd ed.; Springer: Berlin, 1998. pp 57–134.
- (43) Storr, G. J.; Haneman, D. Surface Recombination Velocity and Barrier Width from Surface Photovoltaic Measurement. *J. Appl. Phys.* **1985**, *58*, 1677–1679.
- (44) Asada, M. Intraband Relaxation-Time in Quantum-Well Lasers. *IEEE J. Quantum Electron.* **1989**, *25*, 2019–2026.
- (45) Rossi, F.; Kuhn, T. Theory of Ultrafast Phenomena in Photoexcited Semiconductors. *Rev. Mod. Phys.* **2002**, *74*, 895–950.